Non-linear or linear propagation in high intensity blasts from firearms: where is the boundary?

G. Billot [1], B.G. Marinus [1], K. Harri [1], F. Moiny [2]
[1] Royal Military Academy, Department of Mechanical Engineering,
Rue Hobbema 8, 1000, Bruxelles, Belgium
e-mail: **Guido.Billot@mil.be**

[2] UMONS, Faculty of Engineering, General Physics Unit,
Rue de Houdain, 9, 7000, Mons, Belgium

Abstract

Acoustic nonlinearity increases the degree of modelling complexity but is nevertheless necessary to fully capture the time-frequency content of an impulsive event. Both national and international standards commonly deployed to predict free-field outdoor sound propagation from firearms (ISO 9613, NT Acou 099, ISO 17201) not only neglect nonlinear phenomena, but also fail in providing a clear-cut methodology to discriminate between linear and nonlinear regimes. Correctly establishing the extent of the transition region between the nonlinear and linear solvers allows to optimize the prediction strategies, by allocating the right computational resources where most needed. The present study attempts to make clarity on the subject by observing the evolution of key metrics in the propagation of blasts from small and large caliber weapons. On-field test campaigns were carried out to obtain the datasets needed for the analysis and the free-field propagation of the muzzle blast is simulated with a Nonlinear Progressive Wave Equation solver.

1   Introduction

Nonlinearity in the equations governing fluid dynamics becomes of importance whenever the acoustic pressure exceeds certain levels of magnitude and the impossibility of linearization adds an additional layer of complexity. At such acoustic pressures, the sound waves perturb the surrounding air leading to different propagation speeds in different parts of the wave. When the shock wave discontinuity begins, a cascade of higher frequencies is generated and phenomena such as wave steepening, shock coalescence, frequency redistribution and anomalous energy dissipation might occur. Improving the scientific knowledge of such dynamics has direct impact on the continuity of strategical training activities, personnel well-being and community noise abatement measures. Extensive literature has been produced on the topic of nonlinear sound propagation. The study of underwater blasts was pioneered by *McDonald et al.* ([1] [2] [3]), *Muhlestein et al.* [4] applied a model based on the weak-shock theory to predict the peak pressure evolution after the explosion of gas-filled balloons and *Leissing* [5] formulated an analytical model to predict the transition from nonlinear to linear acoustic regime for a specific class of signals. Steady-state signals like military jet-noise were studied ([6], [7] [8]) in an attempt to identify and measure nonlinearities with parameters such as the skewness of the time derivative of the pressure waveforms and the average steepening factor (ASF) and *Averiyanov* [9] conducted laboratory-scale investigations of N-waves produced by electrical sparks. However, outdoor acoustic propagation is inseparable from medium inhomogeneities, atmospheric absorption, diffractive phenomena and ground effects. The real behavior of the waveform largely departs from that of the ideal N-wave, making purely theoretical predictions and laboratory-scale experiments incomplete. The impulsive nature of gun shots invalidates the use of some of the metrics typically used for continuous sounds and different thresholds seem to mark the onset of nonlinearity: 134 [dB], 130 [dB], 154 [dB] ([10], [11], [12]). The present work addresses these deficiencies by conducting

quantitative observations of nonlinearities from an experimental dataset of two weapons and comparing it with numerical predictions. The discussion is articulated around the evolution with the propagation distance of two metrics: peak intensity and frequency content. Power spectral density (PSD) and Fourier transform are ideal to describe *stationary* processes but they prove unsuitable for transient processes that unfold within the span of a few milliseconds. A wavelet-based analysis is instead proposed, allowing a more accurate decomposition of the signal characteristics that preserves the time-frequency resolution.

Sec.2 contains a detailed description of the equipment used during field tests and of the arrangement of the sensors. **Sec.3** briefly introduces the numerical model and its practical implementation for the cases under examination. In **Sec. 4**, the results of the numerical simulations are illustrated and commented, with a focus on the third-octave bands analysis whereas in **Sec. 6** conclusions are drawn and directions for the continuation of this research are outlined.

2   Experimental campaigns

Two experimental campaigns were conducted at the same military base and involved two different firearms: the Browning Hi-Power 9 mm and Giat LG1 Howitzer 105 mm. For the sake of readability, the latter will be from now onwards referred to as LCW (large caliber weapon) whereas the former as SCW (small caliber weapon).

The complete measurement system consists of four GRAS 46BG 1/4" pressure microphones (Frequency range: 3.15 Hz - 70 kHz, Dynamic range: 60 dB - 184 dB), one PCB 378C10 1/4" (Frequency range: 5 Hz – 70 kHz, Dynamic range: 50 dB - 173 dB) and three GRAS 46AM 1/2" free-field microphones (Frequency range: 3.15 Hz – 31.5 kHz, Dynamic range: 25 dB - 149 dB). The sampling is performed at 70 [kHz] by an 8-channels National Instruments PXI-4492 module mounted on a NI PXIe 1082 chassis. The analogue signal is transferred by coaxial cables and digitized by a custom LabVIEW script while the raw data entirely processed with MATLAB. Pressure and free-field microphones were oriented respectively at 90° and 0° with respect to the propagation direction of the acoustic rays and are mounted on 1.5 [m] tall tripods. The height from the ground of the muzzle of the SCW and LCW is respectively 1.5 [m] and 3 [m]. All sensors are equipped with foam windscreens to avoid excessive background disturbances.

Table 1 – Meteorological conditions

	T_{am} [K]	P_{am} [Pa]	RH [%]	Wind*	Receivers' direction*
LCW	290.15	101250	67.9	3.4 [m/s] (293°, WNW)	70°
SCW	286.65	102700	64.8	3.3 [m/s] (320°, NW)	343°

*All directions are indicated with respect to North

The atmospheric conditions (Table 1) for the LCW are recorded by an on site real-time weather station and averaged over the recording period. Since this infrastructure was not in place for the SCW tests, meteorological data were obtained from the closest local station. Although the average wind direction was never aligned with the propagation lines, the conditions can be altogether regarded as upwind for the SCW and moderately downwind for the LCW. Both the propagation paths stretch along a grassy and mostly flat terrain, with occasional irregularities and dunes not exceeding 1 [m] height. A 2 [m] tall protection wall (Fig. 1) partially delimited the left side of the SCW's microphones' line, introducing reflective components in the measured signals. A series of 5 single shots for the SCW and 3 single shots for the LCW was recorded and used in the post-processing.
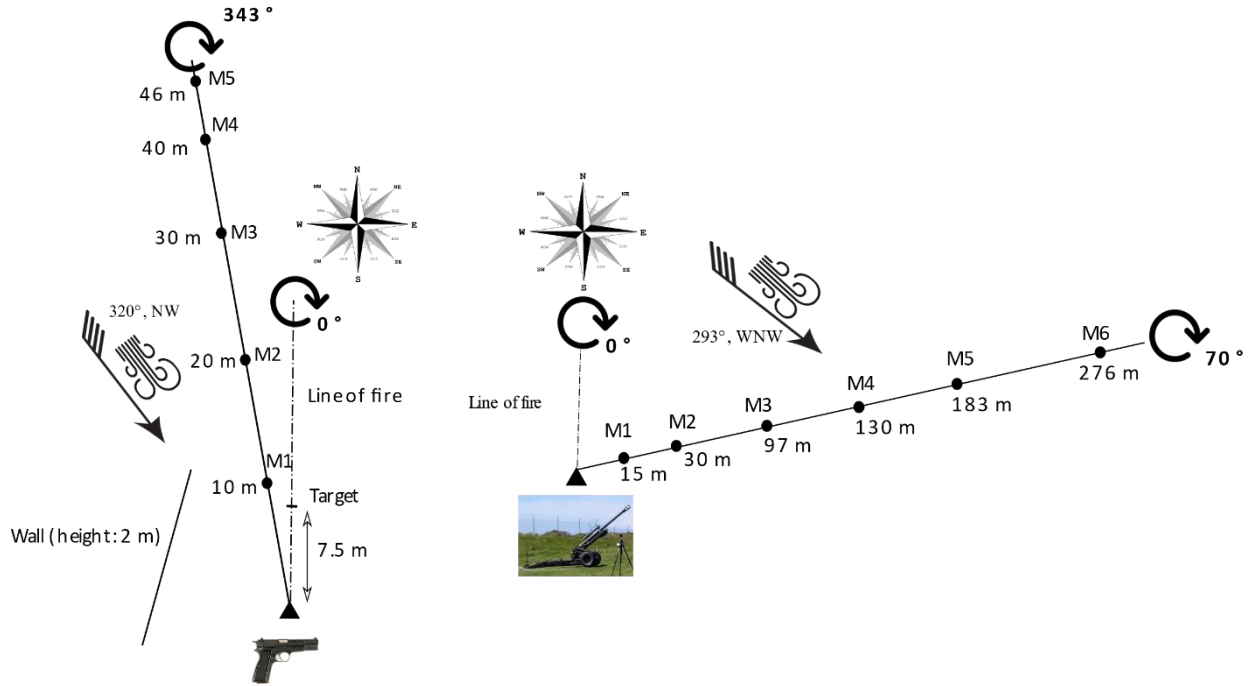
Figure 1: Experimental setup. Left: SCW. Right: LCW

3 Nonlinear Progressive Wave Equation (NPE)

The Nonlinear Progressive Wave Equation was originally developed [1] to study underwater high-intensity acoustic phenomena known as caustics. Due to its modularity and its capacity to accurately resolve weakly nonlinear shockwaves travelling along a principal direction, the model was applied to atmospheric propagation of explosions [10], jet sonic booms [13] and muzzle blasts [14]. Although extended formulations are available [15], the canonical form of the NPE can only accurately resolve shockwaves within 10° from the main propagation direction. The equation is cast in a wave-following reference frame that travels with the ambient speed of sound c_0.

The version implemented here ([16], [15]) is expressed in axisymmetric cylindrical coordinates (r, z), a simplification legitimized by the interest in the acoustic field near the ground.

$$\partial_t R = -\frac{c_0}{2}\frac{R}{r} - \partial_r\left(c_1 R + c_0 \frac{\beta}{2} R^2\right) - \int \left[\frac{c_0}{2}\partial_z^2 R\right] dr + \frac{1}{2}\delta_{eff}\left(\frac{\partial^2}{\partial r^2} + \frac{1}{r}\frac{\partial}{\partial r}\right)R - \frac{1}{\tau}R \tag{1}$$

where

$$R = \frac{\rho'}{\rho_0} \approx p'/(\rho_0 c_0^2) \tag{2}$$

The primed variables (ρ', p') indicate the state of perturbation with respect to the initial undisturbed condition (ρ_0, p_0, c_0) and the dimensionless acoustic pressure (R) is the only scalar unknown. The cylindrical coordinate $r = c_0 t + x$ describes the total propagation distance, where x is the position *within* the moving window.

Proceeding in order, the right-hand side includes a cylindrical decay term, refraction, nonlinearity, diffraction, atmospheric absorption and an artificial operator designed to ensure a non-reflective upper boundary. The coefficient of nonlinearity for air is $\beta = \frac{1+\gamma}{2} = 1.2$ and is the scale factor for the quadratic

dependency on pressure that drives the nonlinear waveform steepening. The effective damping coefficient includes both thermoviscous and relaxational losses [17] ($\delta_{\text{eff}} = \delta_{\text{cl}} + \delta_{\text{rel}} = 1.67 \times 10^{-3}$ [m^2/s]).
Eq. 1 is solved with a time-marching finite difference algorithm where each member of Eq. 1 is solved sequentially, updating the temporary intra-step solution computed by the previous block (Fig. 2)
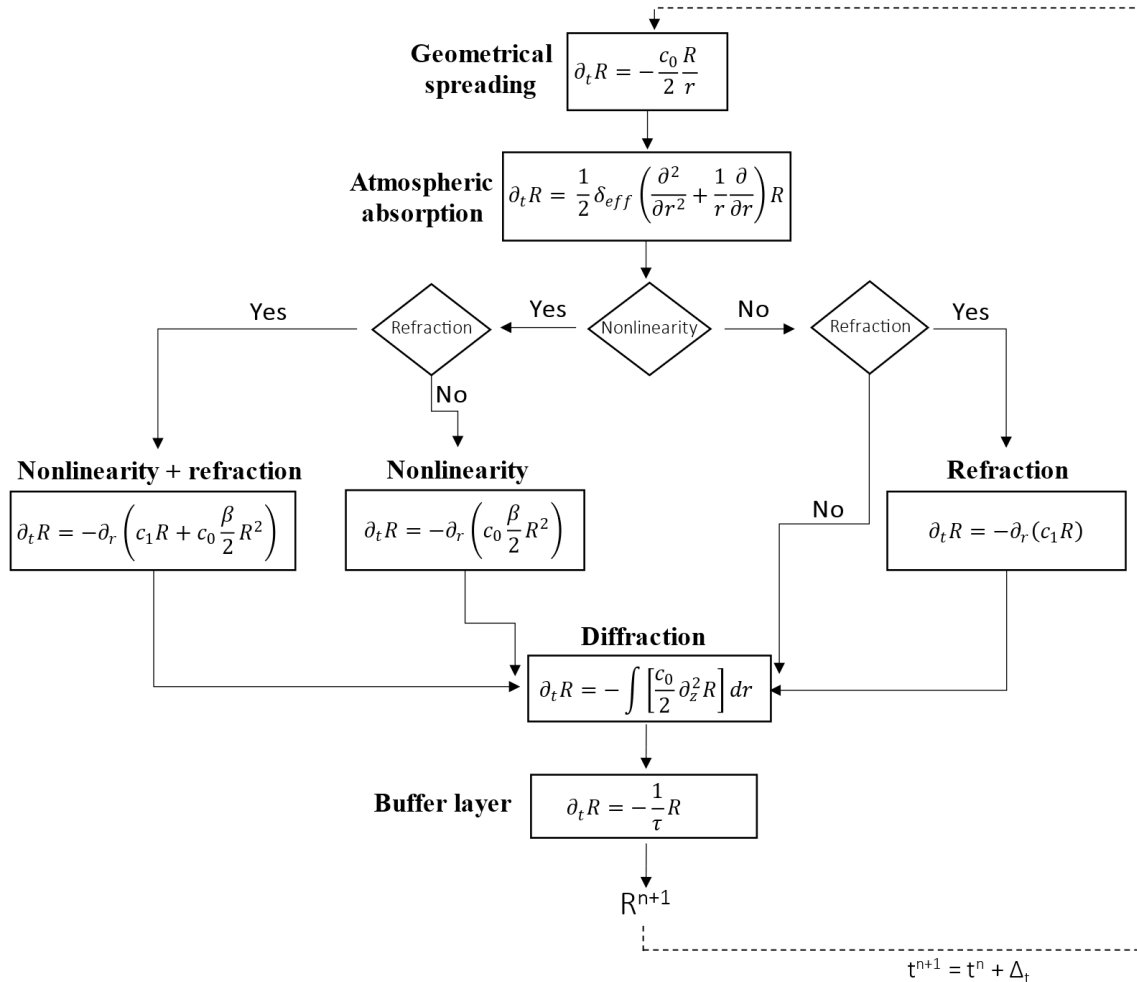
Figure 2: Simplified flowchart of the NPE 2D operator splitting method at the nth time iteration

The nonlinear term is solved with a Flux Corrected Transport [18] method, designed to be second-order accurate, monotone, conservative and able to preserve positivity. This numerical scheme has been previously validated with Fubini's analytical solution [19]. The remaining terms are discretized with the implicit Crank-Nicholson scheme.

3.1 Numerical setup

The domain is discretized by a structured rectangular grid with an aspect ratio $\left(\frac{\Delta_z}{\Delta_r}\right)$ of 5 ([15], [20], [21]) and the window advances of one radial grid spacing at every time step ($\Delta_t = \frac{\Delta_r}{c_0}$). In order to obtain the 2D initial distribution of acoustic pressure shown in Fig. 3, a 1D analytical Friedlander waveform [22] modelled around the measured curve is radially interpolated, the muzzle of the gun being at the center of this field.
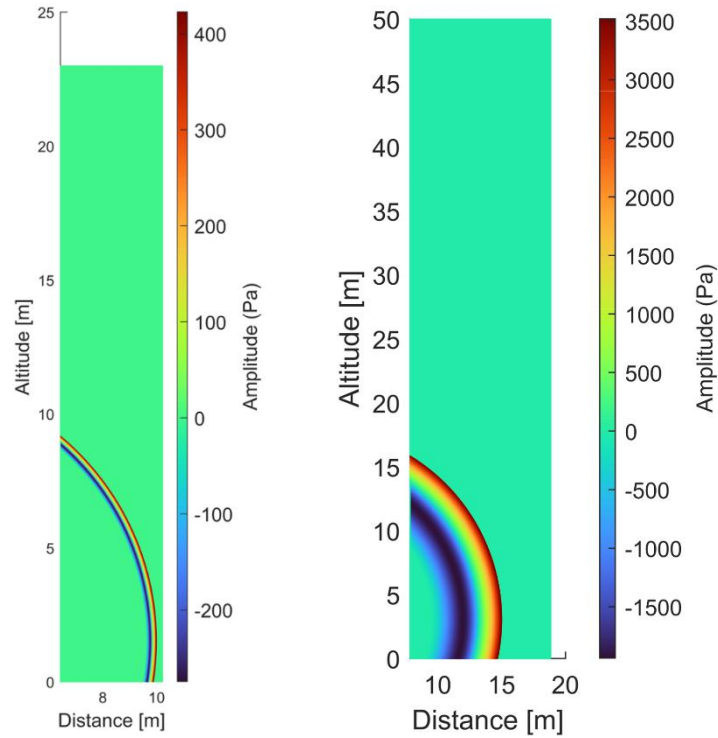

Figure 3: Acoustic pressure fields at t = 0 [s]. *Left:* SCW. *Right:* LCW

The size of the numerical window is chosen to ensure that the wavefront remains within the lateral boundaries throughout the entire simulation (Table 2). This requires and additional operator to enforce a tapered profile of absorption providing a gradual damping of the acoustic field, becoming total for the upper row of the grid [5] (Fig. 4). An empirical tuning process revealed that a buffer layer occupying the upper 20% of a sufficiently tall domain coupled with a 5th order polynomial profile ($\beta_{abs} = 5$) was sufficient to prevent any spurious reflection from the top boundary to pollute the region of interest. For lack of a detailed wind profile characterization, a generic logarithmic profile was adopted (Fig. 4) and the parameter *b* adjusted to match the averaged measured wind speed at the source height.

Table 2: Numerical setup for the two simulations

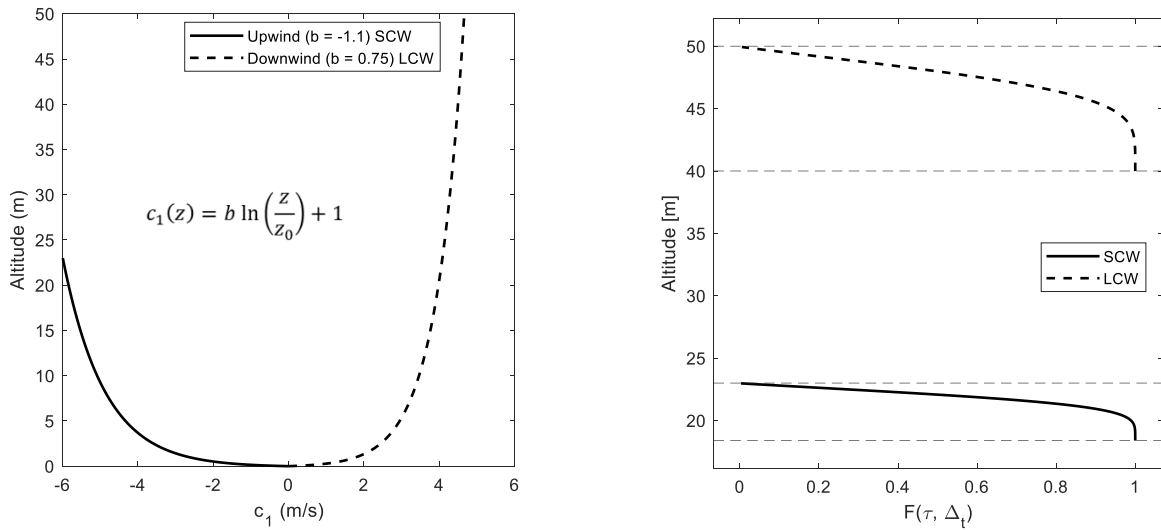|	Δ_r [mm]	Δ_z [mm]	Δ_t [ms]	N_r	N_z	N_t
LCW	8.5	42.5	0.024	1295	1176	34374
SCW	3.5	17.5	0.01	1086	1314	55309

Figure 4: *Left:* logarithmic wind gradient profiles. *Right:* coefficient of absorption for the buffer layer

The boundary condition at the bottom of the domain describes a reflective rigid ground and is enforced by modifying the lowest row of the matrix system obtained by discretizing the diffraction term with a Crank-Nicholson method, as described in [5]. The assumption that the perturbation is absent far enough on the sides of the impulse signal allows for a straightforward treatment of the lateral boundary conditions:

$$R_{1,j}^n = 0, \quad j = 1, \dots, N_z \quad \forall n$$

$$(3)$$

$$R_{N_r,j}^n = 0, \quad j = 1, \dots, N_z \quad \forall n$$

4   Results

The metric chosen to investigate the frequency domain behavior is the Z-weighted one third-octave band sound exposure level (SEL):

$$L_E = 10 \log \left(\frac{1}{T_0} \int_{-\infty}^{+\infty} \frac{p^2(t)}{p_0^2} \, dt \right) \tag{4}$$

The squared pressure signal $p^2(t)$ is integrated over its temporal duration and normalized by the squared reference sound pressure ($p_0 = 20 \, \mu\text{Pa}$) and a reference duration $T_0 = 1$ [s]. This metric is considered suitable when studying impulsive events and has the advantage of eliminating the influence of the measurement duration. To complement the SEL, the continuous 1-D wavelet transform is computed with the analytic Morse wavelet, to provide an immediate interpretation of the time and frequency evolution of non-stationary signals.

The effect of nonlinearity on the frequency spectrum is well known [23] and can be observed in the measured spectra.
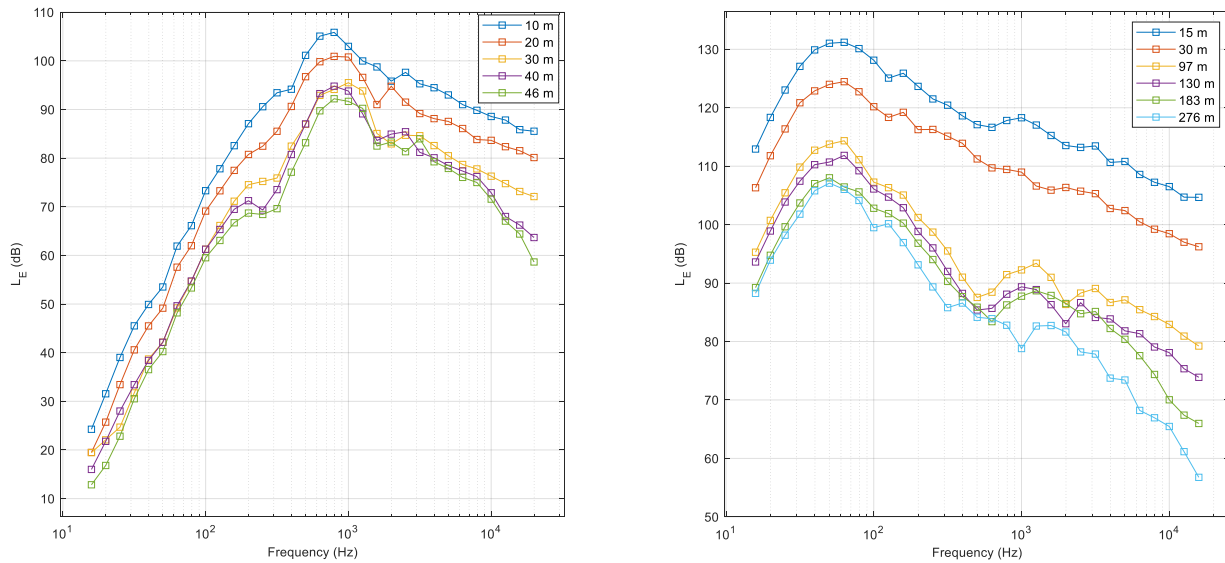
Figure 5: Averaged measured spectra for the SCW *(left)* and the LCW *(right)*

The local increase in entropy caused by nonlinear steepening acts as a dissipation mechanism that depletes the initial energy carried by the signal's principal harmonic and transfers it to a newly formed cascade of higher frequencies. Two physical mechanisms compete to shape the acoustic content of the signal at high frequencies. In the near-field, nonlinearity is predominant and contributes to preserving the high frequency spectrum. As the propagation distance increases, the amplitude of the signal is attenuated and nonlinear effects are expected to subside, making way for linear atmospheric absorption. The definition of near-field is entirely dependent on the caliber, the loading and the weapon's mode of detonation. Looking at Fig. 5, the high frequency spectra exhibit a constant slope at high frequencies up to 30 [m] for the SCW and up to 130 [m] for the LCW. Beyond these distances, a roll-off at high frequencies results in a downward bending of the curves whose onset differs of an order of magnitude: 10 [kHz] for the SCW and 1 [kHz] for the LCW. The trough forming in the 100 [Hz] – 200 [Hz] range of the LCW curves is a combination of the effect of finite ground impedance, aggravated by the wind-driven downward refraction of the acoustic rays [24], and nonlinear frequency redistribution.

In order to isolate the effects of nonlinearity, the numerical fields in Fig. 3 are propagated with fully nonlinear ($\beta = 1.2$) and fully linear ($\beta = 0$) versions of the 2D solver described in **Sec. 3**. Virtual receivers were positioned at the measurement locations depicted in Fig.1, at 1.5 [m] (SCW) and 3 [m] (LCW) altitude from the numerical ground layer. Due to the constant speed c_0 of the moving window, the recovery of the time domain signals is straightforward and is followed by the application of 6th order Butterworth third-octave filter banks to obtain the L_E spectra.

The experimentally obtained one-third octave band SEL are computed as the arithmetical mean of all the recorded signals and the confidence bounds span from the minimum to the maximum level. In addition to numerically simulated results, the ISO-17201's [12] predictions are included. Their validity is restricted to weapons with smaller than 20 [mm] caliber and to distances where peak pressures are less than 1 [kPa] (L_{peak} < 154 [dB]). It does not come as a surprise that the standard performs well for the SCW (Fig. 6). The background noise appears to overshadow SCW's frequency content up to 100 [Hz], whereas the peak in the LCW's range above 10 [kHz] is likely due to external interference from the generator or another electronic device. Its intermittent nature is especially visible near the ceiling of the wavelet transform at 183 [m], in the form of periodic low energy pulses, lasting throughout the entire measurement period.
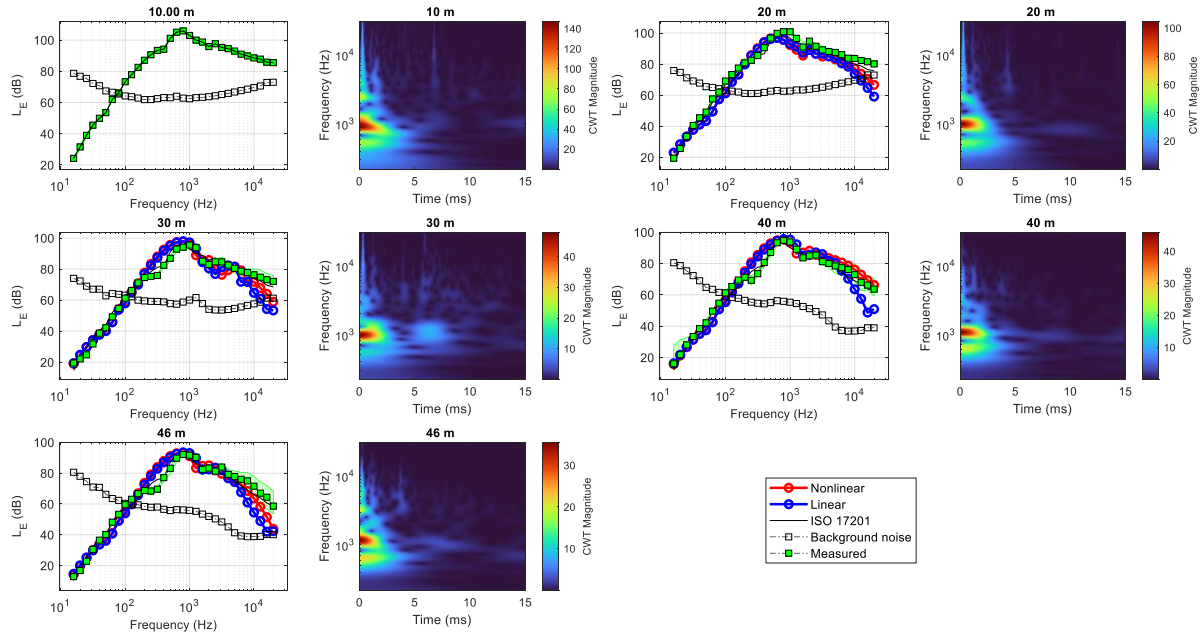
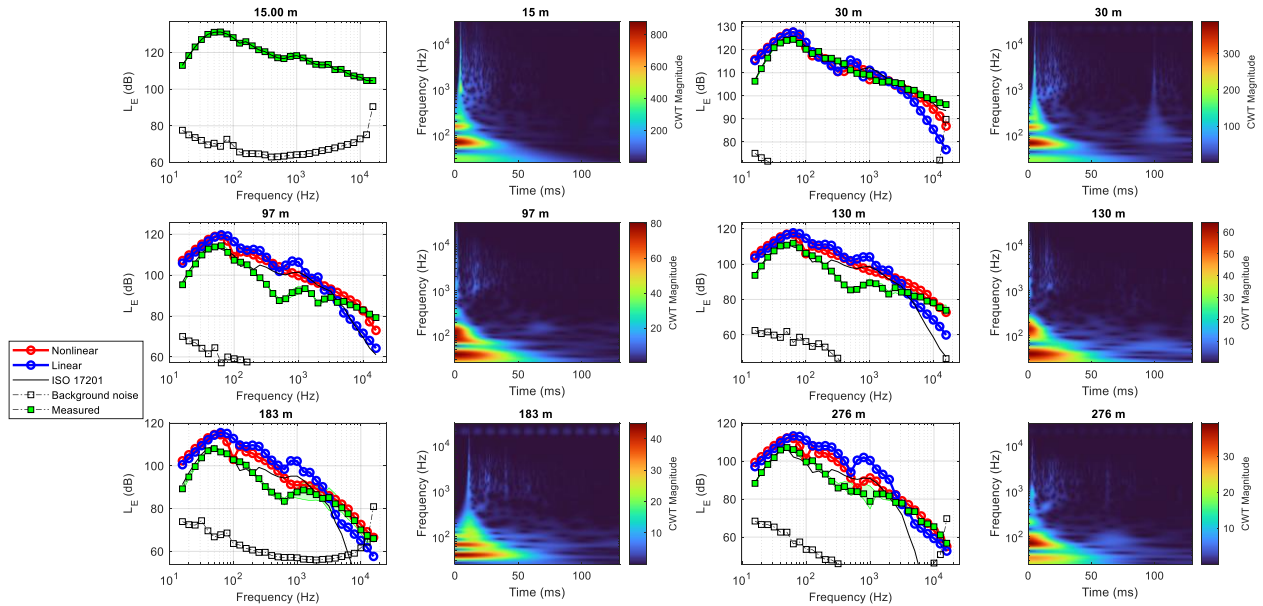Figure 6: Sound Exposure Level (SEL) and continuous wavelet transform for the SCW

Figure 7: Sound Exposure Level (SEL) and continuous wavelet transform for the LCW

Both nonlinear and linear solution underpredict SCW's measured spectra (Fig. 8), except for the 40 [m] position. The small gap between the nonlinear and linear results suggests a moderate nonlinearity that does not yield any major low frequency reshaping. The wavelet-transform (Fig. 6) coefficients display a neat vertical band at frequencies up to and beyond 10 [kHz]. The upper part of this band slowly degrades for the 40 [m] and 46 [m] plots. The time domain footprint of the SCW reveals the lack of any substantial distortion and confirms the small contribution of the low frequencies in the energy content. The low intensity ripples occurring downstream of the pulse are linked to the terrain conformation and tend to be confined to the 1000 [Hz] range.
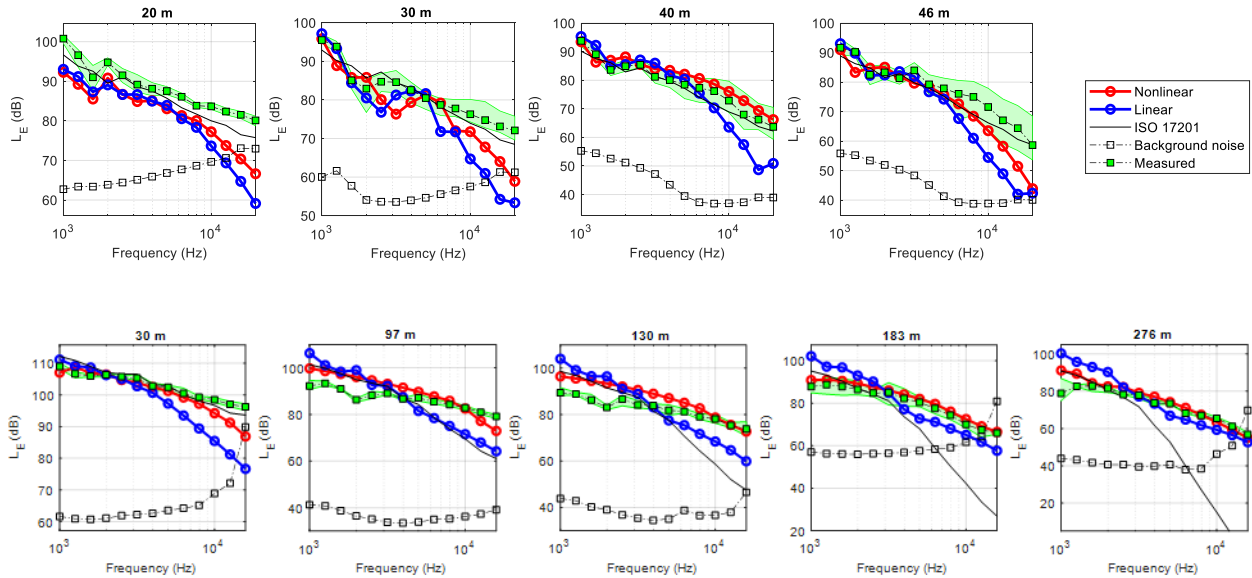
Figure 8: Zoomed view of the SEL at frequencies above 1 [kHz]. *Top:* SCW *Bottom:* LCW

Looking at Fig. 8, the drop in the levels predicted by ISO-17201 [12] after 30 [m] stands out for the LCW, leading to a 40 [dB] error in tracking the experimental curve at high frequency. The purely nonlinear solution provides a superior performance above 1000 [Hz]. However, the gap with the linear results shrinks with propagation distance, falling consistently below 5 [dB] at 276 [m]. It becomes evident at 183 [m] that the nonlinear curve captures the flattening of the spectrum centered around 1000 [Hz] better than both the linear solution and the standard prediction. Unlike for the SCW, the steepening of the time domain curve is now noticeable from the spreading of low energy content in the wavelet transform plots (Fig.7).
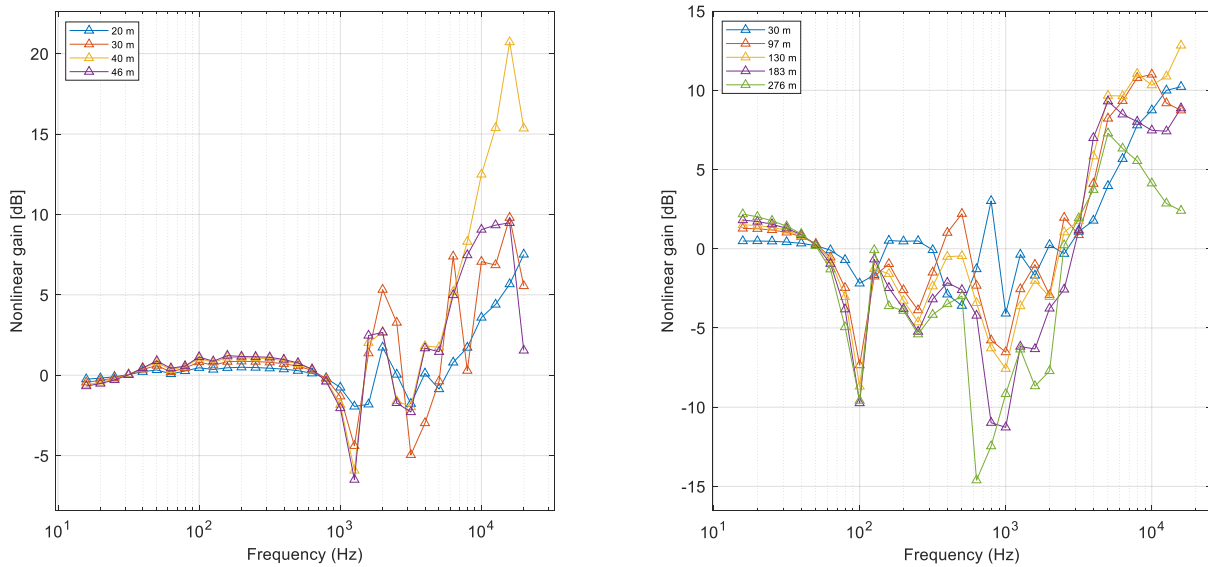

Figure 9: Nonlinear gain *Left:* SCW. *Right:* LCW

By defining the nonlinear gain ($L_E^{nonlinear} - L_E^{linear}$) as an indicator of the presence of nonlinearities, the previous observations can be condensed in a compact way (Fig.9). A negative gain reveals a loss of energy in the nonlinear solution in favour of higher frequencies. The SCW shows virtually no gain up to 1000 [Hz], and the negative portion of the plot hardly exceeds –5 [dB]. Two distinguished energy transfer zones can be identified looking at the LCW's gain. The first one is centered around 100 [Hz] and the second one around 1000 [Hz]. For both the small and large calibers the gain drops below the 5 [dB] level beyond 10 [kHz],

respectively at 46 [m] and at 276 [m]. These results indicate that the nonlinearity effects predictably weaken with distance but still persists even after the high frequency roll-off of the experimental spectra (Fig. 5) is triggered and reinforced by atmospheric absorption.
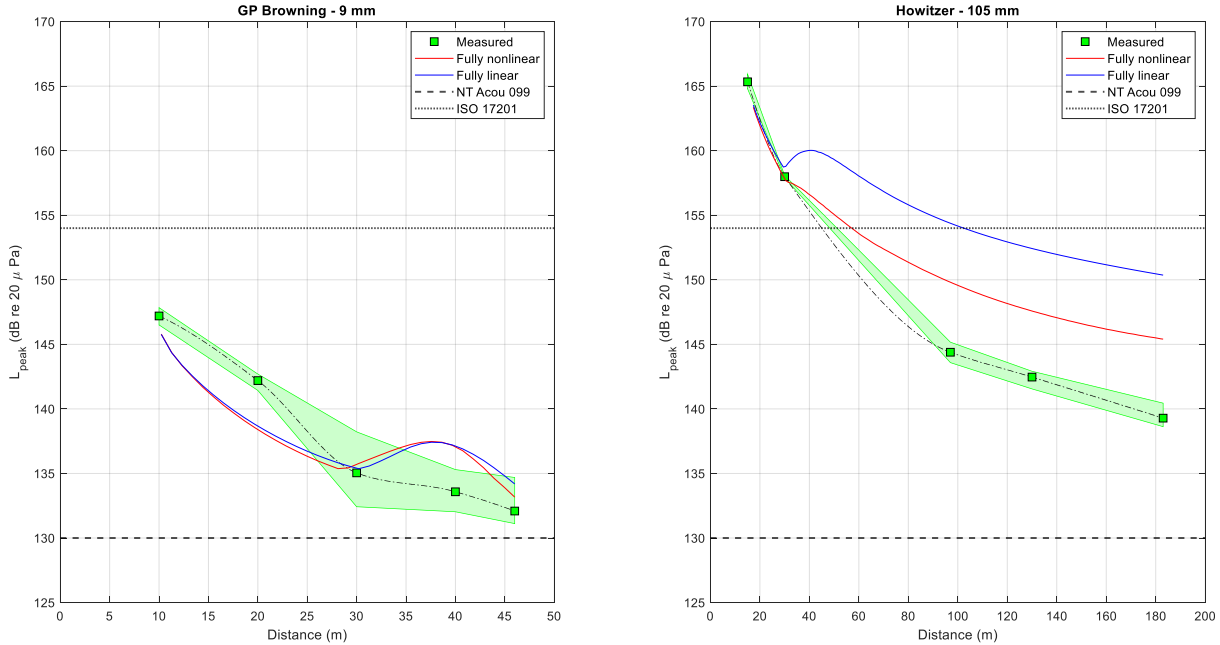

Figure 10: Peak amplitude decay with distance

The discrepancy with the measured values observed in Fig.10 might come from the fact that cylindrical spreading underestimates the real geometrical attenuation to a degree which is difficult to quantify in retrospect. The use of the operator splitting technique implies that at each time step all the attenuation mechanisms affect and are affected by the others.

The information extracted from the frequency domain points to an alternative interpretation of the ISO-17201's L_{peak} threshold. The limit of 154 [dB] does not mark the transition to a linear regime but rather defines a correlation with the intensity of nonlinear effects. If the source is located above this limit, there is evidence in the frequency domain that the nonlinear effects are more intense, long-lasting and outside of the scope of a linear solver. Fig. 10 shows an almost negligible (< 1 [dB]) gap between the nonlinear and linear results for the SCW.

5 Conclusions

Real world experimental conditions make it difficult to establish a clear-cut location where nonlinearity ceases to show its effects. It is perhaps more reasonable to identify a transition region where there is evidence of the weakening of nonlinear mechanisms. For the SCW, a weak energy transfer observed in both the experimental and the numerical predictions, the small difference between the nonlinear and linear solutions, and the good performance of the ISO-17201 standard suggest this region could be defined between 30 [m] and 50 [m].

On the other hand, the LCW maintains its high frequency energy content up to approximately 100 [m]. Inclusion of more calibers in the experimental dataset is a mandatory step to consolidate the effectiveness of the NPE solver and the claims of a correlation between the 154 [dB] limit and the intensity of nonlinearities. Limited cabling capacity, the natural constraints posed by the environment of the shooting ranges and safety measures all represent important restrictions to far-field investigation. Being able to experimentally observe the time-frequency signature of the waveform over larger distances might guarantee

more solid conclusions on the weakening of nonlinear effects. Conducting a similar analysis for different propagation directions could open an interesting discussion about the directivity effect on the transition to a linear regime.

Acknowledgements

References

[1] B. E. McDonald, and W. A. Kuperman, "Time domain formulation for pulse propagation including nonlinear behavior at a caustic," *The Journal of the Acoustical Society of America*, vol. 81, pp. 1406-1417, 1987, https://doi.org/10.1121/1.394546

[2] B. E. McDonald, P. Caine, and M. West, "A Tutorial on the Nonlinear Progressive Wave Equation (NPE) - Part 1," *Applied Acoustics*, vol. 43, pp. 159-167, 1994, https://doi.org/10.1016/0003-682x(94)90059-0

[3] B. E. McDonald, and W. A. Kuperman, "Time-domain solution of the parabolic equation including nonlinearity," *Computer & Mathematics with Applications*, vol. 11, pp. 843-851, 1985, https://doi.org/10.1016/0898-1221(85)90179-8

[4] K. L. G. Muhlestein, and J. H. Macedone, "Educational demonstration of a spherically propagating acoustic shock," *The Journal of the Acoustical Society of America*, vol. 131, pp. 2422-2430, 2012, https://doi.org/10.1121/1.3676730

[5] T. Leissing, "Nonlinear outdoor sound propagation. A numerical implementation and study using the nonlinear progressive wave equation", MSc Dissertation, Chalmers University of Technology, Sweden, 2006.

[6] K. L. Gee, T. B. Neilsen, J. M. Downing, M. M. James, R. L. McKinley, R. C. McKinley, and A. T. Wall, "Near-field shock formation in noise propagation from a high-power jet aircraft,", vol. 133, no. 2, pp. EL88-EL93, 2013, https://doi.org/10.1121/1.4773225

[7] K. L. Gee, et al. "Comparison of two time-domain measures of nonlinearity in near-field propagation of high-power jet noise," in *20th AIAA/CEAS Aeroacoustics Conference*, 2014, https://doi.org/10.2514/6.2014-3199

[8] B. O. Reichman, "Time-Domain Characterization of Nonlinear Propagation in Military Aircraft Jet Noise", PhD Dissertation, Brigham Young University, USA, 2018.

[9] M. Averiyanov, "Propagation des ondes acoustiques à travers un milieu turbulent: Etudes théorique et expériementale des effets de diffraction et des effets non linéaire", PhD Disertation, Ecole centrale de Lyon, France, 2008.

[10] T. Leissing, "Nonlinear acoustic wave propagation in complex media : application to propagation over urban environments", PhD Dissertation, Université Paris-Est, France, 2009.

[11] Nordtest Method [NT], Shooting Ranges : Prediction of Noise (NT Acou 099), 2002.

[12] Acoustics - Noise from shooting ranges - Part 1: Determination of muzzle blast by measurement (NBN EN ISO 17201-1:2019).

[13] V. S. Locey and A. Piacsek, "Sonic boom post processing to include atmospheric turbulent effects," in *14th AIAA/CEAS Aeroacoustics Conference (29th AIAA Aeroacoustics Conference)*, 2008, https://doi.org/10.2514/6.2008-3035

[14] F. van der Eerden, and E. Védy, "Propagation of shock waves from source to receiver," *Noise Control Engineering journal*, vol. 53, pp. 87-93, 2005, https://doi.org/10.3397/1.2839248

[15] B. E. McDonald, "High-angle formulation for the nonlinear progressive-wave equation model," *Wave Motion*, vol. 31, pp. 165-171, 2000, https://doi.org/10.1016/s0165-2125(99)00044-x

[16] G.-P. J. Too and J. H. Ginsberg, "Cylindrical and spherical coordinate versions of NPE for transient and steady-state sound beams," in *Transactions of the ASME*, 1992, https://doi.org/10.1115/1.2930279

[17] A. A. Piacsek, "Atmospheric turbulence conditions leading to focused and folded sonic boom wave fronts," *The Journal of the Acoustical Society of America*, vol. 111, pp. 520-529, 2002, https://doi.org/10.1121/1.1377631

[18] J. P. Boris, A. M. Landsberg, E. S. Oran, and J. H. Gardner, *LCPFCT-A flux-corrected transport algorithm for solving generalized continuity equations*. 1993, https://doi.org/10.21236/ada265011

[19] G. Billot, B. G. Marinus and K. Harri, "Weakly Nonlinear Pulse Propagation in Large Caliber Weapons: a Time-Domain Approach based on the Nonlinear Progressive Wave Equation," in *Proceedings of Euronoise 2021*, 2021.

[20] G. P. J. Too, and S. T. Lee, "Thermoviscous effects on transient and steady-state sound beams using nonlinear progressive wave equation models," *The Journal of the Acoustical Society of America*, vol. 97, pp. 867-874, 1995, https://doi.org/10.1121/1.412131

[21] A. Piacsek and K. Plotkin, "SCAMP: Application of Nonlinear Progressive-wave Equation to sonic boom transition focus," in *51st AIAA Aerospace Sciences Meeting including the New Horizons Forum and Aerospace Exposition*, 2013, https://doi.org/10.2514/6.2013-1064

[22] S. Rigby, A. Tyas, T. Bennett, and S. Clarke, "The Negative Phase of the Blast Load," *International Journal of Protective Structures*, vol. 5, pp. 1-19, 2014, https://doi.org/10.1260/2041-4196.5.1.,

[23] A. D. Pierce, *Acoustics - An Introduction to Its Physical Principles and Applications*. Springer, Ed., ASA PRESS, 2019, https://doi.org/10.1007/978-3-030-11214-1

[24] T. Markula, "Propagation, measurement and assessment of shooting noise," 2006.

[25] International Organization for Standardization [ISO], Acoustics - Attenuation of sound during propagation outdoors - Part 1 : Calculation of the absorption, 1996.

Appendix

A Nomenclature

∂_i	Partial derivative with respect to variable i
β	Coefficient of hydrodynamic nonlinearities
β_{abs}	Polynomial coefficient for the absorption profile
δ_{eff}	Effective sound diffusivity coefficient
δ_{cl}	Thermoviscous losses contribution to sound diffusivity
δ_{rel}	Relaxational losses contribution to sound diffusivity
Δ_r	Spatial step in the radial (x) direction
Δ_z	Spatial step in the vertical (z) direction
Δ_t	Time step
ρ_0	Ambient air density
p'	Perturbed acoustic pressure with respect to the ambient value
p_0	Ambient pressure
P_{am}	Ambient pressure
ρ'	Perturbed air density with respect to the ambient value
b	Scaling factor for the magnitude of wind speed gradient
c_0	Ambient sound speed
c_1	Spatially varying sound speed perturbation
j	Index for grid points in the z-direction
L_E , SEL	Sound exposure level
L_{peak}	Peak sound pressure level
n	Time step index
N_r	Number of grid points in the r-direction
N_z	Number of grid points in the z-direction
N_t	Number of time steps
$p(t)$	Pressure signal in time domain
r	Coordinate describing the radial propagation direction from the source
R	Dimensionless acoustic pressure perturbation
T_0	Reference duration of 1 [s]
T_{am}	Ambient temperature
x	Position within the computational window
z	Coordinate describing the vertical dimension of the domain
LCW	Large caliber weapon
NW	Northwest
NPE	Nonlinear Progressive Wave Equation

RH   Relative humidity

SCW   Small caliber weapon

WNW   West-northwest